Title

Underestimated MJO Variability in CMIP6 Models

Permalink

https://escholarship.org/uc/item/9gm930pq

Journal

Geophysical Research Letters, 48(12)

ISSN

0094-8276

Authors

Le, Phong VV
Guilloteau, Clément
Mamalakis, Antonios
et al.

Publication Date

2021-06-28

DOI

10.1029/2020gl092244

Peer reviewed

Underestimated MJO Variability in CMIP6 Models

Phong V. V. Le[1,2] (ID), **Clément Guilloteau**[1], **Antonios Mamalakis**[1,3] (ID), **and Efi Foufoula-Georgiou**[1,4] (ID)

[1]Department of Civil and Environmental Engineering, University of California-Irvine, Irvine, CA, USA, [2]Faculty of Hydrology Meteorology and Oceanography, University of Science, Vietnam National University, Hanoi, Vietnam, [3]Department of Atmospheric Science, Colorado State University, Fort Collins, CO, USA, [4]Department of Earth Systems Science, University of California-Irvine, Irvine, CA, USA

Abstract The Madden-Julian Oscillation (MJO) is the leading mode of intraseasonal climate variability, having profound impacts on a wide range of weather and climate phenomena. Here, we use a wavelet-based spectral Principal Component Analysis (wsPCA) to evaluate the skill of 20 state-of-the-art CMIP6 models in capturing the magnitude and dynamics of the MJO. By construction, wsPCA has the ability to focus on desired frequencies and capture each propagative physical mode with one principal component (PC). We show that the MJO contribution to the total intraseasonal climate variability is substantially underestimated in most CMIP6 models. The joint distribution of the modulus and angular frequency of the wavelet PC series associated with MJO is used to rank models relatively to the observations through the Wasserstein distance. Using Hovmöller phase-longitude diagrams, we also show that precipitation variability associated with MJO is underestimated in most CMIP6 models for the Amazonia, Southwest Africa, and Maritime Continent.

Plain Language Summary Dominant modes (i.e., coherent spatio-temporal patterns of variability) of the climate system, such as the Madden-Julian Oscillation (MJO), influence a wide range of weather and climate phenomena worldwide. The ability of state-of-the-art climate models to accurately simulate these modes is crucial for advancing our understanding of the climate system and reliably predicting its future trends. The Coupled Model Intercomparison Project Phase 6 (CMIP6) will be the foundation for the upcoming Intergovernmental Panel on Climate Change (IPCC) Sixth Assessment Report (AR6). Here, we use a wavelet-based spectral principal component analysis (wsPCA) to quantitatively assess how well historical simulations from 20 CMIP6 models capture MJO as compared to the observations. We first show that the MJO magnitude is not reproduced well in most of CMIP6 models. We then reveal that MJO-related precipitation variability in the Amazonia, Southwest Africa, and Maritime Continent is significantly underestimated in many CMIP6 models. Our results highlight the need to better simulate the coupled ocean-atmosphere dynamics in order to improve the representation of MJO in climate models and increase confidence in projected states of MJO for assessing future tropical and extratropical impacts.

1. Introduction

The Madden-Julian Oscillation (MJO) is the dominant mode of intraseasonal (1–3 months) variability in the tropical atmosphere, characterized by an eastward-moving band of rain clouds (Madden & Julian, 1971, 1972). The MJO interacts with a wide range of tropical weather and climate phenomena, including monsoonal systems (Lorenz & Hartmann, 2006; Taraphdar et al., 2018), tropical cyclone activity (Bessafi & Wheeler, 2006; Klotzbach, 2010; Maloney & Hartmann, 2000), and the El Niño-Southern Oscillation (ENSO) (Hendon et al., 2007; Lau & Waliser, 2012; Lee et al., 2019). As a strong tropical heating source, the MJO also exhibits teleconnections to the extratropics affecting regional hydroclimate (Jones et al., 2004; Roxy et al., 2019). Given the planetary-scale climatic impacts of the MJO, the ability of state-of-the-art coupled general circulation models (CGCMs) to accurately capture its magnitude, location, and dynamics is of vital importance for subseasonal-to-seasonal prediction (Robertson et al., 2015; Woolnough, 2019) and assessment of future global climate (Meehl, Stocker, et al., 2007).

A number of efforts have focused on assessing CGCMs, primarily those participating in the Coupled Model Intercomparison Projects (CMIP) (Lambert & Boer, 2001; Meehl, Covey, et al., 2007; Taylor et al., 2012) in

terms of their ability to properly capture organized spatio-temporal modes across scales. Despite much progress in climate modeling, considerable shortcomings in simulating intraseasonal oscillations (ISOs) and other major modes of climate variability remain, persisting from one model generation to the next (Eyring, Cox, et al., 2019). For instance, previous generation CGCMs typically exhibit poor representation of MJO dynamics both in amplitude and the eastward propagating pattern (Ahn, Kim, Kim, et al., 2017; Hung et al., 2013; Jiang, Waliser, et al., 2015; Lin et al., 2006; Zhang et al., 2006). The primary factors hypothesized to affect MJO simulations in CGCMs include model resolution and physics, especially the air-sea coupling across multiple spatial scales (Jiang, Adames, et al., 2020; Zhang, 2005).

The CMIP6 set of models (Eyring, Bony, et al., 2016) will be the foundation for the IPCC's AR6. Featuring substantial improvements in the physical parameterizations and inclusion of additional Earth system processes, the CMIP6 is expected to provide a rich opportunity to evaluate the aforementioned shortcomings in simulating MJO. Thus far, very few studies have investigated the performance of CMIP6 models in capturing the MJO. Recently, Orbe et al. (2020) analyzed six U.S. climate models participating in CMIP6 and reported improvements in the amplitudes of the MJO-related winds and precipitation compared to the CMIP5. By analyzing 34 models, Ahn, Kim, Kang, et al. (2020) showed that the propagation of MJO over the Maritime Continent in CMIP6 models is more realistic than in the CMIP5. Nevertheless, there is still a general lack of understanding of the MJO representation in the state-of-the-art climate models.

To extract the MJO signal from high-dimensional data sets, we use here the wavelet-based spectral principal component analysis (wsPCA) (Guilloteau et al., 2020). The wsPCA, as other spectral empirical orthogonal function (EOF) analysis methods (Hannachi et al., 2007; Schmidt et al., 2019), relies on the eigen-decomposition of the cross-spectral matrix (CSM) in a desired frequency band. In wsPCA, the CSM is however computed through a complex continuous wavelet transform (CWT), which allows robust spectral and cross-spectral estimation with optimal time-frequency localization while seamlessly removing trends in the data. The wsPCA is designed specifically to extract periodic propagative modes from large spatio-temporal data sets and is therefore suitable for capturing the propagating dynamics of MJO (and other ISOs). The phase (argument) information provided by the complex CWT allows to capture and characterize each propagative mode with a single (complex) eigenvector and associated (complex) PC. The wavelet principal component (wPC) time series resulting from the wsPCA are characterized by their instantaneous magnitude and phase, which are useful quantities to describe the temporal evolution of dynamical climate modes.

In this study, we analyze global precipitation (PPT) and outgoing longwave radiation (OLR) daily time series to assess MJO variability in observations, reanalysis, and as simulated by 20 CMIP6 models under historical forcing. Particularly, we first demonstrate the use of the wsPCA to robustly extract the spatio-temporal patterns of the MJO. We then evaluate the dynamics of MJO simulated in CMIP6 models by comparing them to those inferred by the observations. Finally, we evaluate MJO-related precipitation variability as simulated by CMIP6 models in the Amazonia, Southwest Africa, and Maritime Continent. The rest of this paper is organized as follows. Section 2 describes the data and methodology used. Section 3 presents the main results of this study followed by a summary in Section 4.

2. Materials and Methods

2.1. Data

2.1.1. CMIP6 Models

Daily averaged outputs, including PPT and OLR, from historical simulations of 20 CMIP6 models (Table S1) during the period 1983–2014 are examined. Model output is taken only from the first ensemble member (r1i1p1f1) of each model. All model outputs are bilinearly interpolated to a common equal-area scalable earth (EASE) grid of ~220 km resolution (Brodzik et al., 2014). Anomaly time series of each field are obtained by removing the average of the 15-day period centered on each day of the year from the raw data.

2.1.2. Observations and Reanalysis

For observations, we employ the daily global interpolated OLR obtained from the NCAR. Daily PPT is obtained from the PERSIANN-CDR database (Ashouri et al., 2015). For reanalysis, daily averaged fields of the above variables are obtained from the ERA5 data sets (Hersbach et al., 2020). Observations

and reanalysis data sets are obtained over the same period (1983–2014) and interpolated onto the same EASE grid as CMIP6 models for comparison. Moreover, daily observed precipitation obtained from other data sets (TRMM, IMERG, GPCP, and CMORPH) is used for comparison with the PERSIANN-CDR (Table S2).

2.2. Methodology

We use the wsPCA (Guilloteau et al., 2020) to identify organized spatio-temporal modes of variability within the intraseasonal timescales. Consider a data set consisting of L time-ordered snapshots of a variable at N gridded locations, $X = (x_1, x_2, .., x_N)^T \in \mathbb{R}^{N \times L}$. The ith row of X, that is $x_i^T = (x_{i,t_1}, ..., x_{i,t_L}) \in \mathbb{R}^L$, represents the time series at the ith location. Meanwhile, the jth column $(x_{1,t_j}, ..., x_{N,t_j})^T \in \mathbb{R}^N$ represents the vectorized snapshot at time t_j. The Morlet CWT of x_i is defined as $w_i(v,t) = \frac{1}{\sqrt{v}} \int_{-\infty}^{+\infty} x_i(\tau) \psi_v'(\tau - t) \, d\tau$, where $\psi_v(t) = \Psi\left(\frac{t}{v}\right)$; the symbol $'$ denotes complex conjugate; Ψ is the Morlet "mother" wavelet defined in simplified form as $\Psi(t) \approx \pi^{-1/4} e^{i2\pi f_0 t} e^{-t^2/2}$; v is the scale parameter; and f_0 is the central frequency of the Morlet mother wavelet (Addison, 2002). We choose $f_0 = \sqrt{1/(2 \ln 2)}$, often used in practice when accurate time localization of the wavelet transform is sought. The scale v is uniquely related to the Fourier frequency $f = \frac{f_0}{v}$, which is the central frequency of the "daughter" wavelet ψ_v. The CWT at frequency f of all x_i can be arranged into a matrix of wavelet coefficients:

$$W_f = \begin{bmatrix} w_1(f,t_1) & \cdots & w_1(f,t_L) \\ \vdots & \ddots & \vdots \\ w_N(f,t_1) & \cdots & w_N(f,t_L) \end{bmatrix} \in \mathbb{C}^{N \times L} \tag{1}$$

The empirical CSM at frequency f is then computed as $S_f = \frac{1}{L-1} W_f W_f' \in \mathbb{C}^{N \times N}$ and its eigen-decomposition constitutes the wsPCA:

$$S_f U_f = U_f \Lambda_f \tag{2}$$

where $\Lambda_f \in \mathbb{R}^{N \times N}$ is the diagonal matrix of the eigenvalues ($\lambda_{i,f}^2 \in \mathbb{R}_+, i = 1, ..., N$) and $U_f \in \mathbb{C}^{N \times N}$ is the matrix of column eigenvectors ($u_{i,f} \in \mathbb{C}^N, i = 1, ..., N$) of S_f, respectively. We note that $tr(\Lambda_f) = tr(S_f)$. As the CSM is defined at each frequency, the eigen-decomposition can be performed independently for each frequency. However, if the sought modes span a desired frequency band, S_f can be integrated over that frequency band before performing the eigen-decomposition. Here we define the ISO band-integrated ($4 \leq f \leq 12$ cpy) CSM as:

$$S_{\text{ISO}} = \int_4^{12} \frac{S_f}{f} df \in \mathbb{C}^{N \times N} \tag{3}$$

The diagonal matrix of eigenvalues and the matrix of column eigenvector of S_{ISO} are $\Lambda_{\text{ISO}} = \text{diag}(\lambda_{i,\text{ISO}}^2 \in \mathbb{R}_+, i = 1, ..., N) \in \mathbb{R}^{N \times N}$ and $U_{\text{ISO}} = (u_{i,\text{ISO}} \in \mathbb{C}^N, i = 1, ..., N) \in \mathbb{C}^{N \times N}$, respectively. For unique solution of the eigen-decomposition, we impose unit L2-norm for each eigenvector and a zero argument to the scalar element with the largest modulus in each eigenvector. The wPC series of wavelet coefficients associated with $u_{i,\text{ISO}}$ at frequency f is calculated as:

$$\kappa_{i,f} = W_f' u_{i,\text{ISO}} \in \mathbb{C}^L \tag{4}$$

and the ISO band-integrated complex wPC series is then defined as:

$$\boldsymbol{\kappa}_{i,\mathrm{ISO}} = \int\limits_{4}^{12} \frac{\boldsymbol{\kappa}_{i,f}}{f} df \in \mathbb{C}^{L} \tag{5}$$

Here, the eigenvectors are represented as maps of complex loading coefficients whose argument characterizes the relative phase shift (i.e., time delays) of the wPC time series between different geographical locations. For the scope of this study, we focus only on the leading mode (first eigenvector and associated PC) which is found to represent the pattern and dynamics of MJO. Yet, we note that our methodology has the potential to extract and analyze other intraseasonal modes (e.g., the boreal summer ISO, Kikuchi et al., 2012) using higher-order PCs.

2.3. MJO Diagnostics

2.3.1. Spectral Energy Within the ISO Frequency Band

The energy distribution of the analyzed signal across frequencies is described by the wavelet power spectral density (PSD):

$$PSD(f) = \frac{f_0}{f} \times \frac{1}{N(L-1)} \sum_{n=1}^{N} \sum_{l=1}^{L} \left| w_n(f,t_l) \right|^2 = \frac{f_0}{f} \times \frac{tr(\boldsymbol{S}_f)}{N} \tag{6}$$

and the energy contained within the ISO frequency band is given by:

$$\overline{PSD}_{\mathrm{ISO}} = \frac{1}{12-4} \int\limits_{4}^{12} PSD(f) df = \frac{f_0}{12-4} \times \frac{tr(\boldsymbol{S}_{\mathrm{ISO}})}{N} \tag{7}$$

The fraction of spectral power contributed by wPC1 at frequency f is:

$$FSP_1(f) = \frac{\lambda_{1,f}^2}{tr(\boldsymbol{\Lambda}_f)} \tag{8}$$

and over the ISO frequency band is:

$$\overline{FSP}_{1,\mathrm{ISO}} = \frac{\lambda_{1,\mathrm{ISO}}^2}{tr(\boldsymbol{\Lambda}_{\mathrm{ISO}})} \tag{9}$$

By comparing $PSD(f)$, $\overline{PSD}_{\mathrm{ISO}}$, $FSP_1(f)$, and $\overline{FSP}_{1,\mathrm{ISO}}$ computed from observations and CMIP6 model outputs, an assessment can be made of the ability of CMIP6 models to reproduce the total variance within intraseasonal timescales and to model the MJO mode with the right contribution to the total intraseasonal variance.

2.3.2. Patterns and Propagation Speed of MJO

Unlike classical PCA for which two eigenvectors and corresponding PCs are needed to capture the MJO (M. C. Wheeler & Hendon, 2004), for wsPCA only the complex eigenvector $\boldsymbol{u}_{1,\mathrm{ISO}}$ and complex wPC series $\boldsymbol{\kappa}_{1,\mathrm{ISO}}$ are needed. Specifically, the maps of $\left| \boldsymbol{u}_{1,\mathrm{ISO}} \right|$ and $\arg(\boldsymbol{u}_{1,\mathrm{ISO}})$ capture the magnitude and phase, respectively, of the MJO pattern. To compare MJO patterns between observations and models, the complex correlation coefficient is calculated as:

$$\rho^{\boldsymbol{u}_{1,\mathrm{ISO}}} = \frac{\boldsymbol{u}_{1,\mathrm{ISO}}^{obs} \cdot \boldsymbol{u}_{1,\mathrm{ISO}}^{\prime\,\mathrm{mod}}}{\left| \boldsymbol{u}_{1,\mathrm{ISO}}^{obs} \right|_2 \cdot \left| \boldsymbol{u}_{1,\mathrm{ISO}}^{\prime\,\mathrm{mod}} \right|_2} \in \mathbb{C} \tag{10}$$

where $|\cdot|_2$ denotes the L2-norm.

The wPC1 series $\boldsymbol{\kappa}_{1,\mathrm{ISO}}$ is used to quantitatively diagnose the magnitude and propagation dynamics of MJO. In the two-dimensional complex space defined by the real and imaginary parts of $\boldsymbol{\kappa}_{1,\mathrm{ISO}}$, we form a wsPCA

MJO index akin to the previous indices (Kiladis, Dias, et al., 2014; M. C. Wheeler & Hendon, 2004). Based on the variable used (i.e., OLR or PPT), we designate this index as the wsPCA-based OLR MJO index (wOMI) or the wsPCA-based PPT MJO index (wPMI), respectively. To allow comparison between models and observations, the wPC1 series ($\kappa_{1,\text{ISO}}$) of each model are normalized by the standard deviation of that obtained from observations. Specifically, we work with:

$$\hat{\kappa}_{1,\text{ISO}} = \frac{\kappa_{1,\text{ISO}}}{\lambda_{1,\text{ISO}}^{\text{obs}} / \sqrt{2}} \in \mathbb{C}^L \tag{11}$$

Note here that $\lambda_{1,\text{ISO}}^{\text{obs}} = \sqrt{2}\sigma_{\Re\left(\kappa_{1,\text{ISO}}^{\text{obs}}\right)} = \sqrt{2}\sigma_{\Im\left(\kappa_{1,\text{ISO}}^{\text{obs}}\right)}$. At any time t, the modulus and argument of $\hat{\kappa}_{1,\text{ISO}}(t)$ define the instantaneous intensity and phase of the MJO, respectively. Since $\arg(\hat{\kappa}_{1,\text{ISO}}(t)) \in [0, 2\pi]$, the eight traditional phases of MJO correspond to angular sectors each spanning over $\pi / 4$ radians in the complex plane. The angular frequency $\omega_{1,\text{ISO}}(t) = \Delta\arg(\hat{\kappa}_{1,\text{ISO}}(t)) / \Delta t$ represents the instantaneous propagation speed of MJO. In the rest of the paper, we only discuss wOMI as the primary MJO index as we will show later that the MJO pattern is reproduced more accurately by models using OLR than PPT.

In order to compare models to observations in term of their ability to capture both the magnitude and instantaneous propagating speed of MJO, we form the bivariate probability density function (PDF) of $\left|\hat{\kappa}_{1,\text{ISO}}(t)\right|$ and $\omega_{1,\text{ISO}}(t)$ for models and observations and compare them using a distance metric. We choose the Wasserstein (or Earth Mover's) distance (WD) (Kantorovich, 2006; Rubner et al., 2000) which is a nonlinear metric defined as the minimal amount of work, or optimal mass transport (Villani, 2008), needed to transform a discrete probability distribution to another. This metric allows to rank CMIP6 models based on their skill to reproduce the magnitude and dynamics of MJO.

3. Results

Figure 1 (a1, b1—top row) shows the power spectral density (PSD) of PPT and OLR for the observations, reanalysis, and 20 CMIP6 models. The PSD indicates that much of the energy of both variables is concentrated within the ENSO timescale (2–7 years), highlighting the dominant influence of this interannual variability mode on the climate system. At intraseasonal timescales (1–3 months), the PSD obtained from the multi-model ensemble (MME) mean of PPT is comparable to that from the observations, whereas the PSD of OLR in CMIP6 models is generally higher than that of observations and reanalysis.

The fraction of spectral power contributed by wPC1 (FSP_1) is presented in Figure 1 (a2, b2—bottom row). We note that FSP_1 is high at low-frequencies (interannual and lower frequencies) for both PPT and OLR (40–70% of the spectral power is contributed by wPC1 within the ENSO timescale). At intraseasonal timescales, the FSP_1 of OLR ranges from 4% to 18% and that of PPT is slightly lower. Nevertheless, while the observations and reanalysis show a well-defined peak in FSP_1 within the intraseasonal timescales (reaching up to 16.2%) indicating a coherent signal of MJO (inset plots), many models substantially underestimate FSP_1 within the intraseasonal timescale and show no well-defined peak. This result implies that, although CMIP6 models do not lack total variance within intraseasonal timescales (Figure 1—top panels), they fail to properly model the MJO mode of variability. Comparisons of the PSD and FSP_1 among observed precipitation products are further shown in Figure S1.

The spatial pattern of $\left|u_{1,\text{ISO}}\right|$ computed from observed OLR shows a coherent spatio-temporal mode spanning from the tropical Indian Ocean to the Western Pacific (Figure 2a) and the pattern of $\arg(u_{1,\text{ISO}})$ shown in Figure 2b clearly indicates eastward propagation, demonstrating the robustness of the wsPCA to identify MJO as the dominant mode in the 4-12-cpy frequency band. The spatial patterns of the magnitude and argument of $u_{1,\text{ISO}}$ of OLR and PPT for all CMIP6 models, reanalysis, and observations are presented in Figures S2–S5 for comparison. Furthermore, the lag-longitude diagrams of the reconstructed OLR and PPT anomalies within the intraseasonal timescale are shown in Figure S6. It can be seen that the average eastward propagation speed of MJO as estimated from the observations, reanalysis, and a large number (13/20) of the models is about 5 m/s. Our results suggest that the majority of CMIP6 models are able to capture
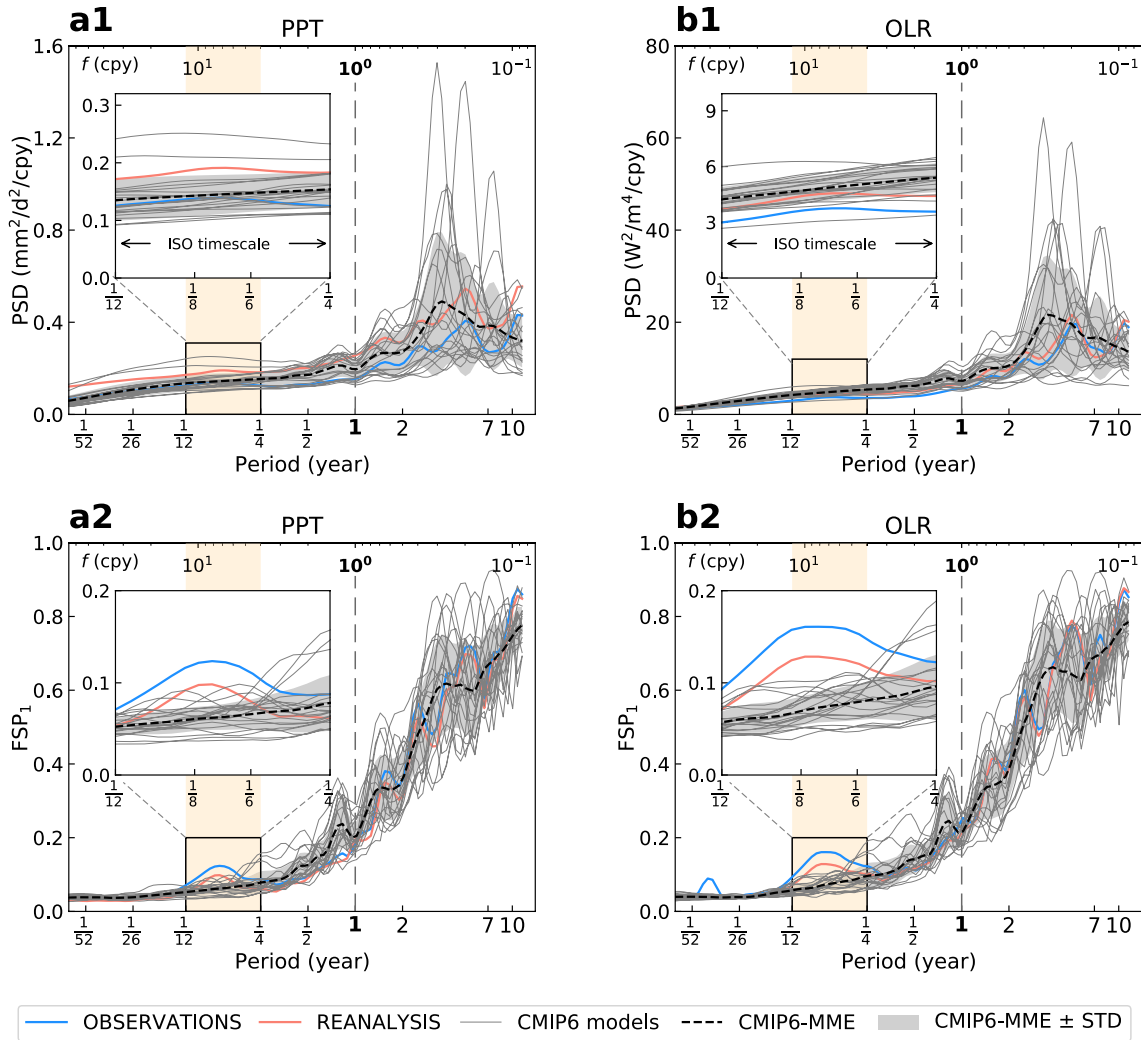
Figure 1. (Top) Power spectral density of (a1) daily precipitation rate (PPT) and (b1) daily outgoing longwave radiation (OLR). (Bottom) Fraction of spectral power explained by wPC1 for (a2) PPT and (b2) OLR. Blue lines correspond to observations, red lines to reanalysis data, dashed black lines correspond to the multimodel ensemble (MME) mean of 20 CMIP6 models, and the gray shaded regions represent MME ± standard deviation (here individual models are not distinguished from one another). Frequency f in cycles per year (cpy) is shown in the top horizontal axes. The timescale corresponding to intraseasonal oscillations (ISO; yellow shaded vertical bands) ranges from 1 to 3 months ($4 \leq f \leq 12$ cpy).

well the average propagation speed of MJO which is consistent with previous studies (Ahn, Kim, Kang, et al., 2020; Orbe et al., 2020). Nevertheless, many models underestimate the MJO variability as reflected by the lower values of the normalized magnitudes $\frac{\lambda_{1,\text{ISO}} \times \sqrt{N}}{\sqrt{tr(\mathbf{\Lambda}_{\text{ISO}})}} |\boldsymbol{u}_{1,\text{ISO}}|$ compared to those of the observations (Figures S2 and S4). The magnitudes of the wPC series $\boldsymbol{\kappa}_{1,f}$ across frequencies and $\hat{\boldsymbol{\kappa}}_{1,\text{ISO}}$ are presented in Figure 2c. These plots show considerable interannual variability and strong seasonality (higher amplitude during boreal winter months) in MJO activity, as also evidenced in Figure 2e by the PDFs of $\hat{\boldsymbol{\kappa}}_{1,\text{ISO}}$ during the winter (November–April) and summer (May–October). Moreover, Figure 2d shows the trajectory in the complex plane of the daily wOMI obtained from observations during the study period and for the boreal winter. The trajectories of daily wOMI and wPMI obtained from all data sets are further presented in Figures S7 and S8.

Comparison of the $\overline{PSD}_{\text{ISO}}$ and $\overline{FSP}_{1,\text{ISO}}$ for PPT and OLR is shown in Figures 3a and 3b, respectively. For PPT, while the CMIP6 models show a spread of the $\overline{PSD}_{\text{ISO}}$ above and below the value of the observations indicating no systematic bias, the $\overline{FSP}_{1,\text{ISO}}$ estimated from the models is consistently smaller
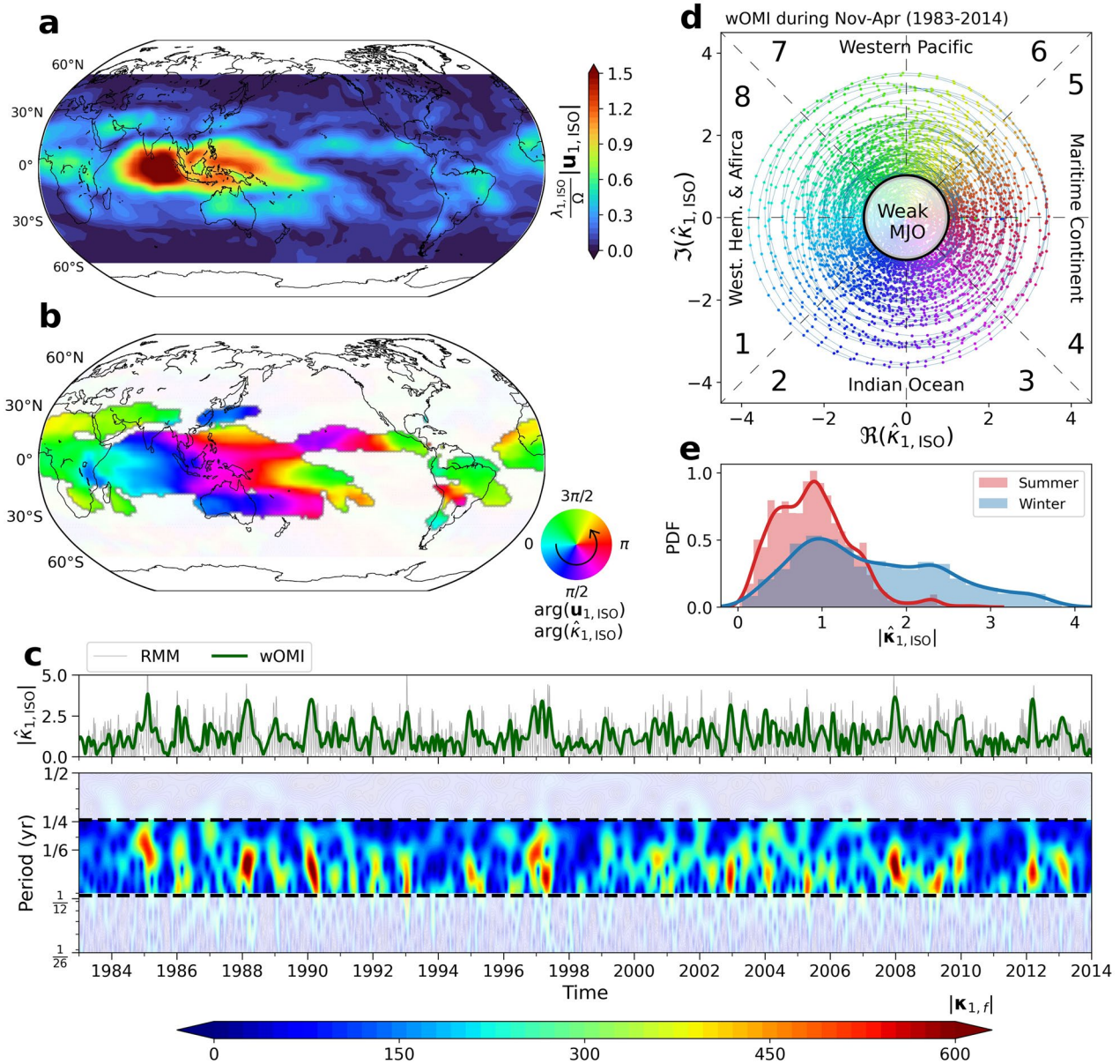
Figure 2. (a and b) Spatial patterns of the intraseasonal oscillation (ISO) band-integrated first complex eigenvector $\boldsymbol{u}_{1,\mathrm{ISO}}$ for observed OLR for (a) modulus (magnitude) and (b) argument (phase), corresponding to MJO. The modulus is shown for the unit-norm eigenvector with a scaling factor $\frac{\lambda_{1,\mathrm{ISO}}}{\Omega}$, with $\Omega = \sqrt{tr(\boldsymbol{\Lambda}_{\mathrm{ISO}})\,/\,N}$. The counter-clockwise, circular arrow in the colorscale indicates the direction of propagation of the extracted wave. (c) Top: Magnitudes of the wsPCA-based OLR MJO index $|\hat{\boldsymbol{\kappa}}_{1,\mathrm{ISO}}|$ (wOMI; green line) and of the real-time multivariate MJO index (RMM; gray line; see M. C. Wheeler and Hendon (2004)). Bottom: Magnitude of the complex wPC1 time series $|\boldsymbol{\kappa}_{1,f}|$ associated with $\boldsymbol{u}_{1,\mathrm{ISO}}$ across frequencies for observed OLR. (d) Trajectory in the complex plane of wOMI ($\hat{\boldsymbol{\kappa}}_{1,\mathrm{ISO}}$) for observed OLR. The wOMI is displayed during boreal winter season (November-April) from 1983 to 2014 with one sample per day plotted. Points that lie inside the black unit circle correspond to days that are classified as weak MJO. The same colorscale as in panel (b) is used to represent the values of $\arg(\hat{\kappa}_{1,\mathrm{ISO}}(t))$, indicating the eastward propagation of MJO. (e) PDFs of wOMI during the boreal winter (November-April) and summer (May-October), demonstrating the ability of wsPCA to capture the seasonality of MJO. See text for definition of variables.

than that from the observations, indicating that the models systematically underestimate the MJO variability. For OLR, most CMIP6 models exhibit higher $\overline{PSD}_{\mathrm{ISO}}$ than observations (except model IP-SL-CM6A-LR(13); Figure 3b); however all models show lower $\overline{FSP}_{1,\mathrm{ISO}}$ than that of the observations, further confirming that CMIP6 models consistently underestimate the contribution of MJO to the intraseasonal climate variability. For both variables, $\overline{PSD}_{\mathrm{ISO}}$ of the reanalysis is slightly higher than
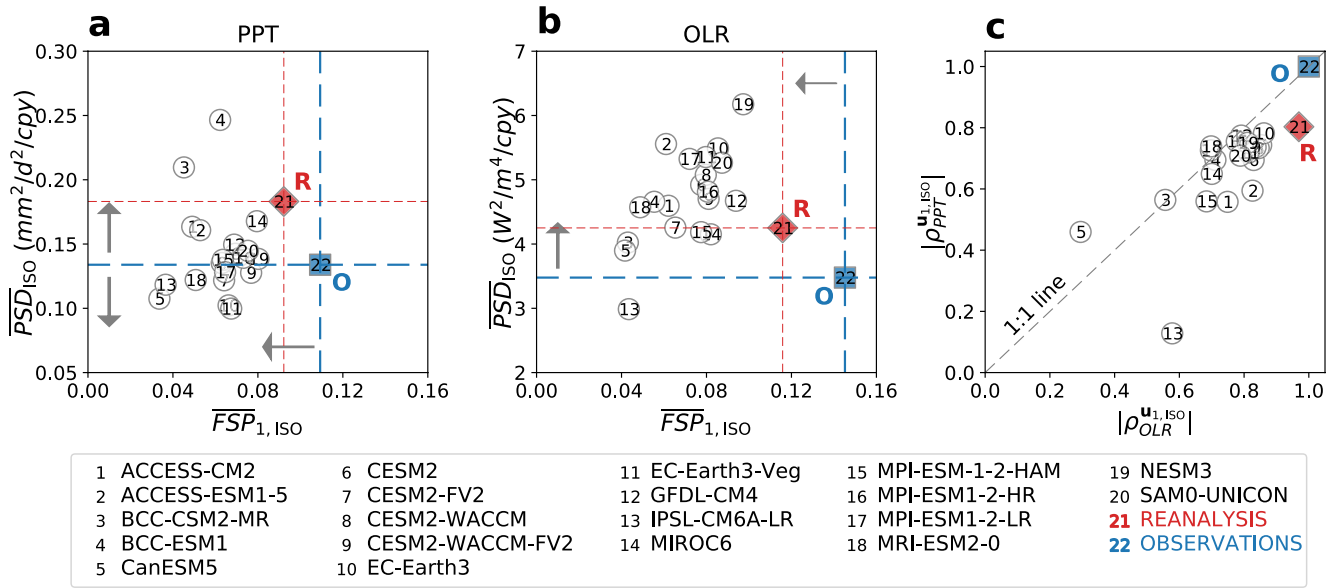
Figure 3. Comparison of spectral energy within the ISO frequency band ($\overline{PSD}_{ISO}$) and the fraction of energy explained by wPC1 ($\overline{FSP}_{1,ISO}$) corresponding to MJO for (a) Precipitation rate and (b) Outgoing longwave radiation for observations, reanalysis products and models. The systematic underestimation of $\overline{FSP}_{1,ISO}$ in the models is apparent. (c) Scatter plot of the correlation coefficients of the patterns for the first complex eigenvectors of the modeled and observed OLR ($|\rho_{OLR}^{u_{1,ISO}}|$) and modeled and observed PPT ($|\rho_{PPT}^{u_{1,ISO}}|$) as defined in Equation 10. Numbers inside markers represent CMIP6 models (1–20), reanalysis (21), and observations (22).

that of the observations, but the $\overline{FSP}_{1,ISO}$ is lower. The scatter plot of the modulus of the complex pattern correlation coefficients $|\rho_{OLR}^{u_{1,ISO}}|$ and $|\rho_{PPT}^{u_{1,ISO}}|$ as defined in Equation 10 is shown in Figure 3c. Most of the models show correlations in the range of 0.6–0.85 for both variables, confirming that, for all models, the first dynamical mode extracted by the wsPCA in the 4-12-cpy frequency band is actually the MJO, and indicating quite good agreement of the modeled MJO patterns to the observed ones. We note however that the complex pattern correlation only indicates agreement between the unit-norm first complex eigenvectors (Equation 10) and does not take into account the discrepancy between their corresponding eigenvalues (variance explained), a discrepancy that has been separately assessed in Figures 3a and 3b. Two models showing very low values of $|\rho_{OLR}^{u_{1,ISO}}|$ and $|\rho_{PPT}^{u_{1,ISO}}|$ are the IPSL-CM6A-LR (13) and CanEMS (5). Finally, most of the scatter points are below the 1 : 1 line, implying that CMIP6 models generally reproduce more accurately the patterns of OLR than PPT.

Figure 4a compares the relationship of the magnitude and propagation speed of MJO for models, reanalysis, and observations for all days during 1983–2014 (these can be seen as joint PDFs). Note that the normalized wPC series $\hat{\kappa}_{1,ISO}$ (see Equation 11) are plotted to allow comparison between models and observations. We find that while the average propagation speed (mean of the PDF of $\omega_{1,ISO}(t)$) is quite similar among all models (0.1 − 0.13 rad/day, equivalent cycles of 60 − 48 days), CMIP6 models underestimate the magnitude $|\hat{\kappa}_{1,ISO}|$ of the MJO mode. The marginal PDFs of $|\hat{\kappa}_{1,ISO}(t)|$ and $\omega_{1,ISO}(t)$ for all data sets are shown in Figure 4b further demonstrating that most of CMIP6 models capture the MJO propagation speed but underestimate the amplitude of MJO compared to the observations (as also shown in Figure 4a). Moreover, Figure 4c shows the ranked WD between the joint PDFs of $|\hat{\kappa}_{1,ISO}(t)|$ and $\omega_{1,ISO}(t)$ inferred by the observations (reference) and those obtained from the reanalysis (red bar) and CMIP6 models (gray bars). The smaller the values of the WD, the better the performance of a model to reproduce the observed MJO magnitude and speed. Relatively good models that show the smallest WD values include the NESM3 (19) and SAM0-UNICON (20) that are consistent with recent reports on the improvements of MJO simulations in these models (Shin & Park, 2020; Yang et al., 2020).

The MJO interacts with a wide range of weather and climate phenomena not only in the tropics but also in the midlatitude regions by its teleconnections (De Souza & Ambrizzi, 2006; Roxy et al., 2019; Sossa
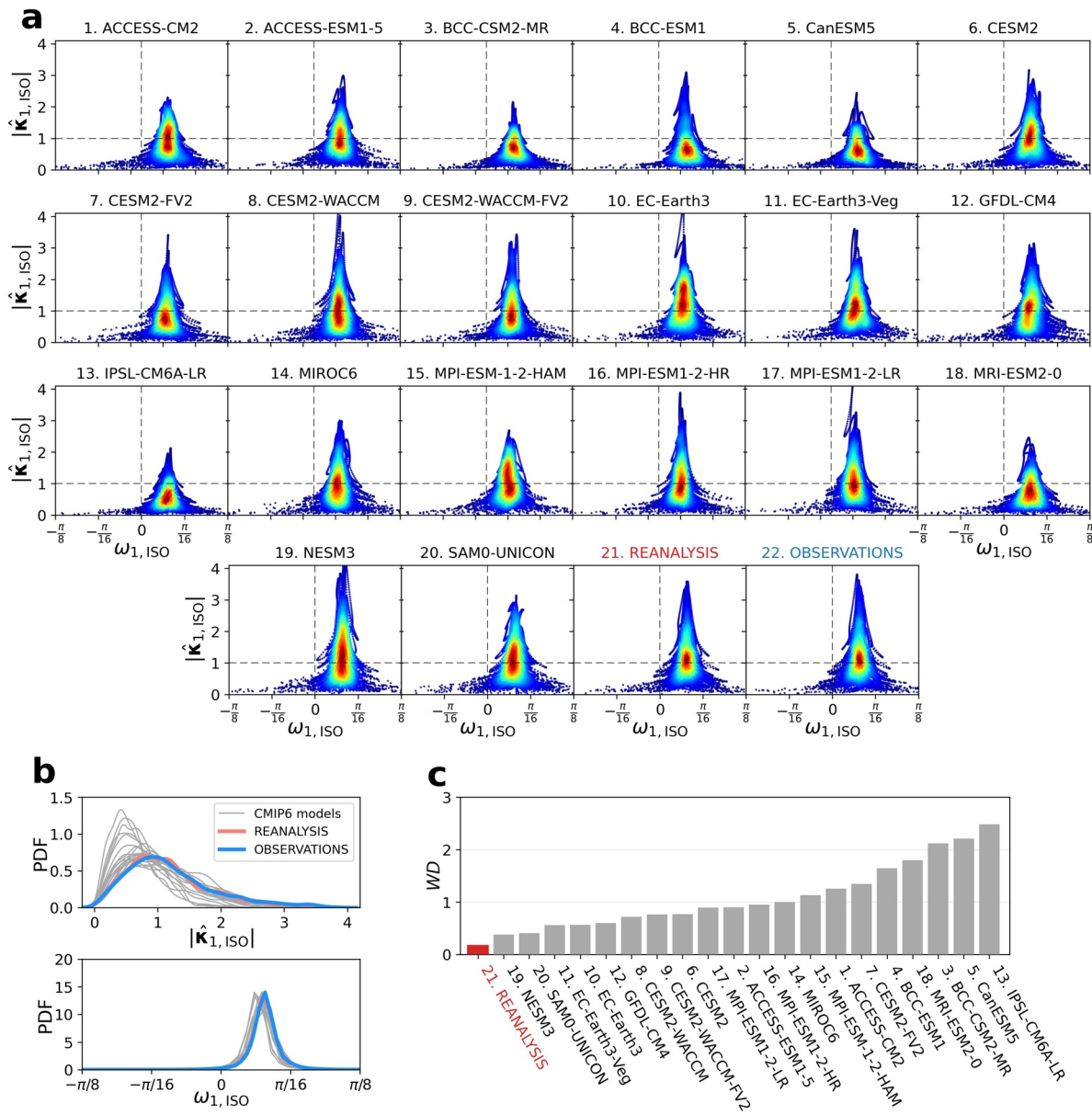
Figure 4. (a) Relationship between the normalized magnitude $|\hat{\kappa}_{1,\mathrm{ISO}}(t)|$ and angular frequency $\omega_{1,\mathrm{ISO}}(t)$ of the ISO band-integrated wPC1 series corresponding to MJO for CMIP6 models, reanalysis products, and observations computed at the daily scale. Points under the unit horizontal dashed lines are classified as weak MJO. The colorscale represents the joint PDF of $|\hat{\kappa}_{1,\mathrm{ISO}}(t)|$ and $\omega_{1,\mathrm{ISO}}(t)$, with warmer color indicating higher probability. (b) Probability density functions of (top) magnitude $|\hat{\kappa}_{1,\mathrm{ISO}}(t)|$ and (bottom) angular frequency $\omega_{1,\mathrm{ISO}}(t)$. (c) Wasserstein distance (WD) between the joint probability distribution of $|\hat{\kappa}_{1,\mathrm{ISO}}(t)|$ and $\omega_{1,\mathrm{ISO}}(t)$ obtained from observations (reference) and those obtained from reanalysis (red bar) and CMIP6 models (gray bars). The WD values of models are sorted from low to high, indicating the ranking of CMIP6 models in reproducing the MJO magnitude and propagation dynamics.

et al., 2017). In Figure 5, we evaluate the impacts of the MJO on precipitation over three different regions: Amazonia, Southwest Africa, and Maritime Continent. The Hovmöller phase-longitude diagrams of PPT anomalies show that the MME mean produces smaller MJO-related precipitation variability compared to the observations during all eight MJO phases and in all regions (Figure 5a). Details of the Hovmöller diagrams for each model in each region are further shown in Figures S9–S11. These diagrams suggest that a large number of CMIP6 models underestimate the MJO signal to regional precipitation compared to the observations. Among three regions, the models produce the most realistic precipitation variability in the Maritime Continent where MJO activity is the greatest. Furthermore, the scatter plots of the WD and cor-
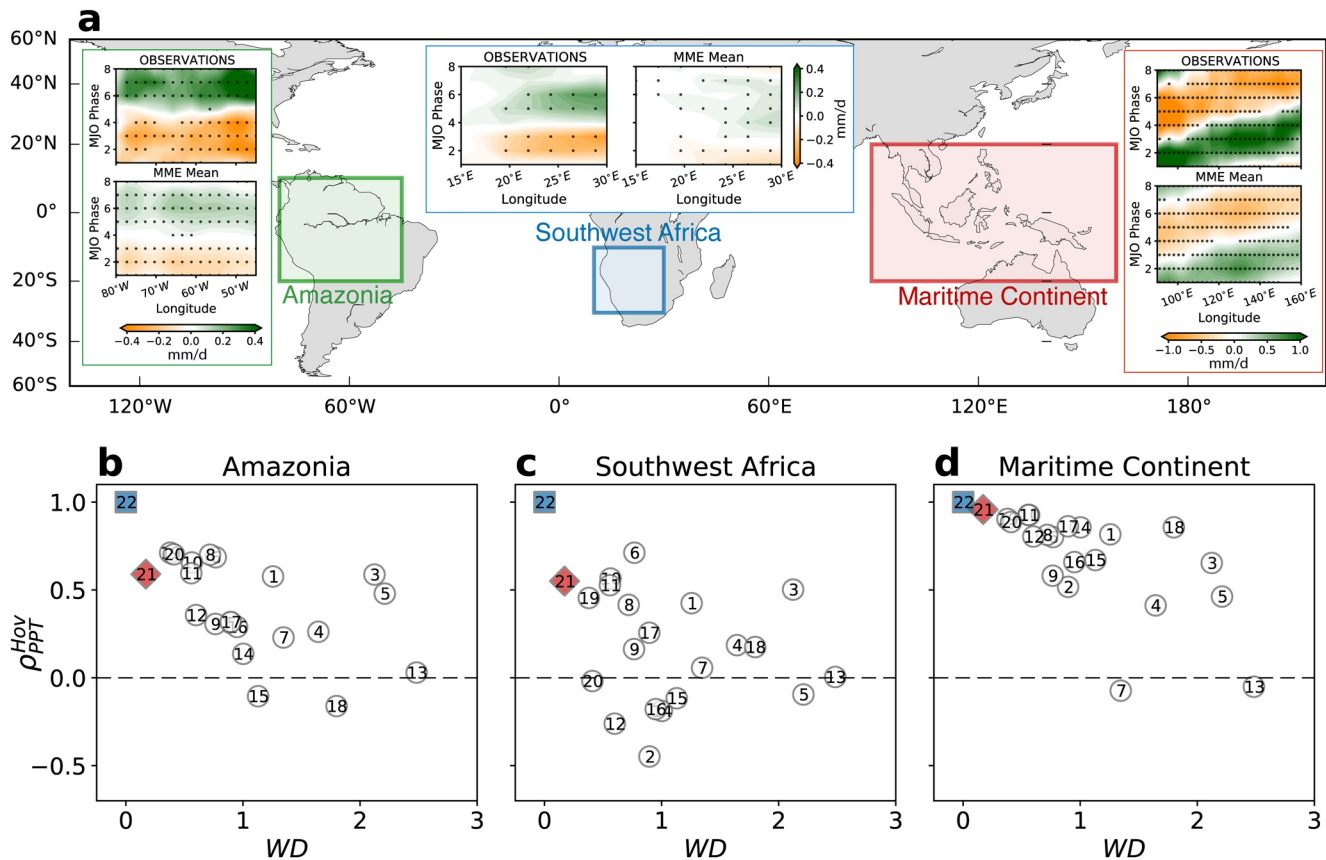
Figure 5. (a, Top) Comparison of modeled (MME Mean) and observed MJO-related precipitation anomalies around the climatic mean over the Amazonia (10°N–20°S, 45°W–80°W), Southwest Africa (10°S–30°S, 15°E–30°E), and Maritime Continent (20°S–20°N, 90°E–160°E). The dots indicate statistically significant anomalies ($p < 0.05$). (Bottom) Scatter plots of the WD between the observed and modeled joint PDFs of $|\hat{\kappa}_{1,\mathrm{ISO}}(t)|$ and $\omega_{1,\mathrm{ISO}}(t)$ (see Figure 4) and the pattern correlation coefficients of the Hovmöller diagram (see Figures S7–S9) between models and observations for the (b) Amazonia, (c) Southwest Africa, and (d) Maritime Continent. Numbers inside markers represent CMIP6 models (1–20), reanalysis (21), and observations (22) as in Figure 3. It is seen that models that better reproduce MJO magnitude and propagation dynamics (low WD value) also tend to better reproduce the MJO-related precipitation variability over Amazonia and Maritime Continent, but not necessarily in Southwestern Africa.

relation coefficients of the Hovmöller diagrams of PPT (ρ_{PPT}^{Hov}) between models and observations for each region are presented in Figures 5b–5d. It can be seen that models showing good performance in reproducing the MJO magnitude (low WD value) also tend to exhibit higher correlation of ρ_{PPT}^{Hov} with observations and larger MJO-related precipitation variability in the Amazonia and Maritime Continent, while this tendency is not observed in Southwestern Africa. Our results suggest that CMIP6 models which underestimate MJO magnitude also reproduce weak MJO teleconnections to regional precipitation.

4. Conclusions

In this study, we have analyzed historical simulations of 20 CMIP6 models to assess their ability to capture the space-time dynamics of MJO. For the first time, we applied the wsPCA to extract the pattern, magnitude, and eastward propagation of MJO from daily PPT and OLR. The key difference of wsPCA compared to other PCA methods is that the CSM between time series across locations is estimated using a complex CWT, enabling robust estimation of the CSM in any desired frequency band. In addition to existing methods in extracting MJO (Giannakis & Majda, 2012; Kiladis, Straub, & Haertel, 2005; Lo & Hendon, 2000; M. C. Wheeler & Hendon, 2004; M. Wheeler & Kiladis, 1999), our approach provides another way to extract MJO in particular and propagating physical modes in general. The wsPCA is also simple to implement without customized parameters, which significantly facilitates the extraction of dynamical modes from a large number of models. We defined the wsPCA MJO indices (wOMI and wMPI) based

on the real and imaginary parts of the ISO band-integrated (4-12-cpy) complex wPC1 series to evaluate the magnitude and phase of the MJO mode at the daily scale and compare models with observations. We then investigated the influence of MJO to precipitation variability in CMIP6 models over three different regions.

The analysis herein showed that most CMIP6 models are able to realistically capture the eastward propagation of MJO as also reported in recent studies (Ahn, Kim, Kang, et al., 2020; Orbe et al., 2020). However, the simulation of the MJO magnitude in CMIP6 remains a challenging problem. We demonstrated that although CMIP6 models exhibit enough spectral power or total variance within the intraseasonal timescales as compared to observations, they tend to underestimate the variability contributed by the MJO mode. This finding encourages potential future research on understanding the contributions of other ISOs to the intraseasonal variability represented in CMIP6 models and previous generation CGCMs. Furthermore, we showed that precipitation variability associated with the MJO is underestimated in the CMIP6 models in the Amazonia, Southwest Africa and Maritime Continent. Our results highlight the need to better simulate the coupled ocean-atmosphere dynamics in climate models to improve the MJO representation and MJO-driven tropical and extratropical rainfall.

Data Availability Statement

The CMIP6 data set is available at https://esgf-node.llnl.gov/projects/cmip6. The ECMWF ERA5 reanalysis data set was downloaded from https://www.ecmwf.int/en/forecasts/datasets/reanalysis-datasets/era5. The PERSIANN-CDR precipitation data was downloaded from https://chrsdata.eng.uci.edu/. The interpolated OLR data of NCAR and the GPCP v2.3 precipitation data were provided by the NOAA/ESRL PSD, Boulder, CO, USA (https://psl.noaa.gov/data/gridded/index.html). The TRMM (34B2) and IMERG precipitation data were provided by the NASA's Precipitation Measurement Missions (https://gpm.nasa.gov/data/directory). The CMORPH precipitation data was provided by the NOAA/CPC (https://www.cpc.ncep.noaa.gov/products/janowiak/cmorph_description.html).

References

Addison, P. S. (2002). *The illustrated wavelet transform handbook: Introductory theory and applications in science, engineering, medicine and finance*. Taylor & Francis. https://doi.org/10.1201/9781420033397

Ahn, M.-S., Kim, D., Kang, D., Lee, J., Sperber, K. R., Gleckler, P. J., et al. (2020). MJO propagation across the maritime continent: Are CMIP6 models better than CMIP5 models? *Geophysical Research Letters*, *47*, e2020GL087250. https://doi.org/10.1029/2020GL087250

Ahn, M.-S., Kim, D., Kim, D., Sperber, K. R., Kang, I.-S., Maloney, E., et al. (2017). MJO simulation in CMIP5 climate models: MJO skill metrics and process-oriented diagnosis. *Climate Dynamics*, *49*(11), 4023–4045. https://doi.org/10.1007/s00382-017-3558-4

Ashouri, H., Hsu, K.-L., Sorooshian, S., Braithwaite, D. K., Knapp, K. R., Cecil, L. D., et al. (2015). PERSIANN-CDR: Daily precipitation climate data record from multisatellite observations for hydrological and climate studies. *Bulletin of the American Meteorological Society*, *96*(1), 69–83. https://doi.org/10.1175/bams-d-13-00068.1

Bessafi, M., & Wheeler, M. C. (2006). Modulation of South Indian Ocean tropical cyclones by the Madden-Julian oscillation and convectively coupled equatorial waves. *Monthly Weather Review*, *134*(2), 638–656. https://doi.org/10.1175/mwr3087.1

Brodzik, M. J., Billingsley, B., Haran, T., Raup, B., & Savoie, M. H. (2014). Correction: Brodzik, M. J., et al. EASE-Grid 2.0: Incremental but Significant Improvements for Earth-Gridded Data Sets. ISPRS International Journal of Geo-Information 2012, 1, 32–45. *ISPRS International Journal of Geo-Information*, *3*(3), 1154–1156. https://doi.org/10.3390/ijgi3031154

De Souza, E. B., & Ambrizzi, T. (2006). Modulation of the intraseasonal rainfall over tropical Brazil by the Madden-Julian oscillation. *International Journal of Climatology*, *26*(13), 1759–1776. https://doi.org/10.1002/joc.1331

Eyring, V., Bony, S., Meehl, G. A., Senior, C. A., Stevens, B., Stouffer, R. J., & Taylor, K. E. (2016). Overview of the Coupled Model Intercomparison Project Phase 6 (CMIP6) experimental design and organization. *Geoscientific Model Development*, *9*(5), 1937–1958. https://doi.org/10.5194/gmd-9-1937-2016

Eyring, V., Cox, P. M., Flato, G. M., Gleckler, P. J., Abramowitz, G., Caldwell, P., et al. (2019). Taking climate model evaluation to the next level. *Nature Climate Change*, *9*(2), 102–110. https://doi.org/10.1038/s41558-018-0355-y

Giannakis, D., & Majda, A. J. (2012). Nonlinear Laplacian spectral analysis for time series with intermittency and low-frequency variability. *Proceedings of the National Academy of Sciences of the United States of America*, *109*(7), 2222–2227. https://doi.org/10.1073/pnas.1118984109

Guilloteau, C., Mamalakis, A., Vulis, L., Le, P. V. V., Georgiou, T. T., & Foufoula-Georgiou, E. (2020). Rotated spectral principal component analysis (rsPCA) for identifying dynamical modes of variability in climate systems. *Journal of Climate*, *34*(2), 715–736.

Hannachi, A., Jolliffe, I. T., & Stephenson, D. B. (2007). Empirical orthogonal functions and related techniques in atmospheric science: A review. *International Journal of Climatology*, *27*(9), 1119–1152. https://doi.org/10.1002/joc.1499

Hendon, H. H., Wheeler, M. C., & Zhang, C. (2007). Seasonal dependence of the MJO-ENSO relationship. *Journal of Climate*, *20*(3), 531–543. https://doi.org/10.1175/jcli4003.1

Hersbach, H., Bell, B., Berrisford, P., Hirahara, S., Horányi, A., Muñoz-Sabater, J., et al. (2020). The ERA5 global reanalysis. *Quarterly Journal of the Royal Meteorological Society*, *146*(730), 1999–2049. https://doi.org/10.1002/qj.3803

Hung, M.-P., Lin, J.-L., Wang, W., Kim, D., Shinoda, T., & Weaver, S. J. (2013). MJO and convectively coupled equatorial waves simulated by CMIP5 climate models. *Journal of Climate*, *26*(17), 6185–6214. https://doi.org/10.1175/jcli-d-12-00541.1

Jiang, X., Adames, Á. F., Kim, D., Maloney, E. D., Lin, H., Kim, H., et al. (2020). Fifty years of research on the Madden-Julian Oscillation: Recent progress, challenges, and perspectives. *Journal of Geophysical Research: Atmospheres*, *125*, e2019JD030911. https://doi.org/10.1029/2019JD030911

Jiang, X., Waliser, D. E., Xavier, P. K., Petch, J., Klingaman, N. P., Woolnough, S. J., et al. (2015). Vertical structure and physical processes of the Madden-Julian oscillation: Exploring key model physics in climate simulations. *Journal of Geophysical Research: Atmospheres*, *120*, 4718–4748. https://doi.org/10.1002/2014JD022375

Jones, C., Waliser, D. E., Lau, K. M., & Stern, W. (2004). Global occurrences of extreme precipitation and the Madden-Julian Oscillation: Observations and predictability. *Journal of Climate*, *17*(23), 4575–4589. https://doi.org/10.1175/3238.1

Kantorovich, L. V. (2006). On the translocation of masses. *Journal of Mathematical Sciences*, *133*(4), 1381–1382. https://doi.org/10.1007/s10958-006-0049-2

Kikuchi, K., Wang, B., & Kajikawa, Y. (2012). Bimodal representation of the tropical intraseasonal oscillation. *Climate Dynamics*, *38*(9), 1989–2000. https://doi.org/10.1007/s00382-011-1159-1

Kiladis, G. N., Dias, J., Straub, K. H., Wheeler, M. C., Tulich, S. N., Kikuchi, K., et al. (2014). A comparison of OLR and circulation-based indices for tracking the MJO. *Monthly Weather Review*, *142*(5), 1697–1715. https://doi.org/10.1175/mwr-d-13-00301.1

Kiladis, G. N., Straub, K. H., & Haertel, P. T. (2005). Zonal and vertical structure of the Madden-Julian Oscillation. *Journal of the Atmospheric Sciences*, *62*(8), 2790–2809. https://doi.org/10.1175/jas3520.1

Klotzbach, P. J. (2010). On the Madden-Julian Oscillation-Atlantic hurricane relationship. *Journal of Climate*, *23*(2), 282–293. https://doi.org/10.1175/2009jcli2978.1

Lambert, S. J., & Boer, G. J. (2001). CMIP1 evaluation and intercomparison of coupled climate models. *Climate Dynamics*, *17*(2), 83–106. https://doi.org/10.1007/pl00013736

Lau, W. K. M., & Waliser, D. E. (2012). El Niño Southern Oscillation connection. In *Intraseasonal variability in the atmosphere-ocean climate system* (pp. 297–334). Berlin: Springer. https://doi.org/10.1007/978-3-642-13914-7_9

Lee, R. W., Woolnough, S. J., Charlton-Perez, A. J., & Vitart, F. (2019). ENSO modulation of MJO teleconnections to the North Atlantic and Europe. *Geophysical Research Letters*, *46*, 13535–13545. https://doi.org/10.1029/2019GL084683

Lin, J.-L., Kiladis, G. N., Mapes, B. E., Weickmann, K. M., Sperber, K. R., Lin, W., et al. (2006). Tropical intraseasonal variability in 14 IPCC AR4 climate models. Part I: Convective Signals. *Journal of Climate*, *19*(12), 2665–2690. https://doi.org/10.1175/jcli3735.1

Lo, F., & Hendon, H. H. (2000). Empirical extended-range prediction of the Madden-Julian Oscillation. *Monthly Weather Review*, *128*(7), 2528–2543. https://doi.org/10.1175/1520-0493(2000)128<2528:EERPOT>2.0.CO;2

Lorenz, D. J., & Hartmann, D. L. (2006). The effect of the MJO on the North American Monsoon. *Journal of Climate*, *19*(3), 333–343. https://doi.org/10.1175/jcli3684.1

Madden, R. A., & Julian, P. R. (1971). Detection of a 40–50 day oscillation in the zonal wind in the tropical Pacific. *Journal of the Atmospheric Sciences*, *28*(5), 702–708. https://doi.org/10.1175/1520-0469(1971)028<0702:DOADOI>2.0.CO;2

Madden, R. A., & Julian, P. R. (1972). Description of global-scale circulation cells in the tropics with a 40–50 day period. *Journal of the Atmospheric Sciences*, *29*(6), 1109–1123. https://doi.org/10.1175/1520-0469(1972)029<1109:DOGSCC>2.0.CO;2

Maloney, E. D., & Hartmann, D. L. (2000). Modulation of Hurricane activity in the Gulf of Mexico by the Madden-Julian Oscillation. *Science*, *287*(5460), 2002–2004. https://doi.org/10.1126/science.287.5460.2002

Meehl, G. A., Covey, C., Delworth, T., Latif, M., McAvaney, B., Mitchell, J. F. B., et al. (2007). THE WCRP CMIP3 multimodel dataset: A new era in climate change research. *Bulletin of the American Meteorological Society*, *88*(9), 1383–1394. https://doi.org/10.1175/bams-88-9-1383

Meehl, G. A., Stocker, T. F., Collins, W. D., Friedlingstein, P., Gaye, A. T., Gregory, J. M., et al. (2007). Global climate projections. In Climate change 2007: The physical science basis (pp. 747–846). Cambridge, UK: Cambridge University Press.

Orbe, C., Van Roekel, L., Adames, Á. F., Dezfuli, A., Fasullo, J., Gleckler, P. J., et al. (2020). Representation of modes of variability in six U.S. climate models. *Journal of Climate*, *33*(17), 7591–7617. https://doi.org/10.1175/jcli-d-19-0956.1

Robertson, A. W., Kumar, A., Peña, M., & Vitart, F. (2015). Improving and promoting subseasonal to seasonal prediction. *Bulletin of the American Meteorological Society*, *96*(3), ES49–ES53. https://doi.org/10.1175/bams-d-14-00139.1

Roxy, M. K., Dasgupta, P., McPhaden, M. J., Suematsu, T., Zhang, C., & Kim, D. (2019). Twofold expansion of the Indo-Pacific warm pool warps the MJO life cycle. *Nature*, *575*(7784), 647–651. https://doi.org/10.1038/s41586-019-1764-4

Rubner, Y., Tomasi, C., & Guibas, L. J. (2000). The Earth Mover's distance as a metric for image retrieval. *International Journal of Computer Vision*, *40*(2), 99–121. https://doi.org/10.1023/a:1026543900054

Schmidt, O. T., Mengaldo, G., Balsamo, G., & Wedi, N. P. (2019). Spectral empirical orthogonal function analysis of weather and climate data. *Monthly Weather Review*, *147*(8), 2979–2995. https://doi.org/10.1175/mwr-d-18-0337.1

Shin, J., & Park, S. (2020). Impacts of ENSO and Madden–Julian oscillation on the genesis of tropical cyclones simulated by general circulation models and compared to observations. *Environmental Research Letters*, *15*(3), 034046. https://doi.org/10.1088/1748-9326/ab7466

Sossa, A., Liebmann, B., Bladé, I., Allured, D., Hendon, H. H., Peterson, P., & Hoell, A. (2017). Statistical connection between the Madden-Julian oscillation and large daily precipitation events in West Africa. *Journal of Climate*, *30*(6), 1999–2010. https://doi.org/10.1175/jcli-d-16-0144.1

Taraphdar, S., Zhang, F., Leung, L. R., Chen, X., & Pauluis, O. M. (2018). MJO affects the monsoon onset timing over the Indian region. *Geophysical Research Letters*, *45*, 10011–10018. https://doi.org/10.1029/2018GL078804

Taylor, K. E., Stouffer, R. J., & Meehl, G. A. (2012). An overview of CMIP5 and the experiment design. *Bulletin of the American Meteorological Society*, *93*(4), 485–498. https://doi.org/10.1175/bams-d-11-00094.1

Villani, C. (2008). *Optimal transport: Old and new*. Berlin: Springer Science & Business Media.

Wheeler, M., & Kiladis, G. N. (1999). Convectively coupled equatorial waves: Analysis of clouds and temperature in the wavenumber-frequency domain. *Journal of the Atmospheric Sciences*, *56*(3), 374–399. https://doi.org/10.1175/1520-0469(1999)056<0374:CCEWAO>2.0.CO;2

Wheeler, M. C., & Hendon, H. H. (2004). An all-season real-time multivariate MJO index: Development of an index for monitoring and prediction. *Monthly Weather Review*, *132*(8), 1917–1932. https://doi.org/10.1175/1520-0493(2004)132<1917:AARMMI>2.0.CO;2

Woolnough, S. J. (2019). The Madden-Julian Oscillation. In A. W. Robertson, & F. Vitart (Eds.), *Sub-seasonal to seasonal prediction* (pp. 93–117). Amsterdam: Elsevier. https://doi.org/10.1016/b978-0-12-811714-9.00005-x

Yang, Y.-M., Wang, B., Cao, J., Ma, L., & Li, J. (2020). Improved historical simulation by enhancing moist physical parameterizations in the climate system model NESM3.0. *Climate Dynamics*, *54*(7), 3819–3840. https://doi.org/10.1007/s00382-020-05209-2

Zhang, C. (2005). Madden-Julian oscillation. *Reviews of Geophysics*, *43*, RG2003. https://doi.org/10.1029/2004RG000158

Zhang, C., Dong, M., Gualdi, S., Hendon, H. H., Maloney, E. D., Marshall, A., et al. (2006). Simulations of the Madden-Julian oscillation in four pairs of coupled and uncoupled global models. *Climate Dynamics*, *27*(6), 573–592. https://doi.org/10.1007/s00382-006-0148-2